

Strain-Gradient-Controlled Disorder Dynamics in Chemically Substituted Ferroelectrics

Peng Tan,¹ Hao Tian,^{1,*} Fei Huang,¹ Xiangda Meng,¹ Yu Wang,¹ Chengpeng Hu,¹ Xilong Cao,¹ Li Li,² and Zhongxiang Zhou¹

¹*Department of Physics, Harbin Institute of Technology, Harbin 150001, China*

²*Key Lab of In-fiber Integrated Optics of Ministry of Education, College of Science, Harbin Engineering University, Harbin 150001, China*

(Received 5 July 2018; revised manuscript received 23 November 2018; published 14 February 2019)

Correlated disorder, a type of crystallographic state, widely exists in complex material systems and is beneficial for the improvement of material properties. The strain gradient ∇S , caused by structural heterogeneity, controls the features of correlated disorder. However, the exact mechanism whereby ∇S controls the disorder dynamics, especially in bulk materials, is still largely unknown, hindering property optimization. We design and achieve a macroscopic ∇S in the $\text{KTa}_{1-X}\text{Nb}_X\text{O}_3$ (KTN) single crystal by the coupling effect of the Nb-composition gradient ∇X and 180° domains near the Curie temperature T_C . The electric-field dependences of the electro-optic (EO) effect are investigated to reveal the ∇S -controlled disorder dynamics. The EO characteristics indicate that the flexoelectric field E_{flexo} caused by ∇S is sufficiently strong to control the local correlated dipoles. Further, it is demonstrated by dielectric, Raman, and absorption spectroscopies that the ∇S in the KTN sample plays a dominant role in the disorder dynamics. At the nanoscale, the large local ∇S , approximately 10^{-3} – 10^{-2} nm⁻¹ in magnitude, caused by random substitutions of B cations, can determine the local structure and dynamics, deeply influencing the properties of materials. This work reveals how ∇S acts on the disorder dynamics and local dipole behaviors, which provides the basis for the understanding and harnessing of disordered ferroelectrics.

DOI: 10.1103/PhysRevApplied.11.024037

I. INTRODUCTION

Correlated disorder, which is a type of crystallographic state, has received considerable attention as it appears more frequently than crystalline phases [1,2]. Materials that exhibit a strongly correlated disorder possess a large number of remarkably strong and malleable magnetic, electric, optical, and mechanical properties [3–9]. Solid-solution perovskites are a classic example of disordered ferroelectric crystals [10,11]. They exhibit large electro-optic (EO) and piezoelectric effects, which are attributed to the presence of polar nanoregions (PNRs) and nanodomains [12–14]. Chemical substitutions and local dipolar distortions in ABO_3 -type lattices are responsible for the dynamics of these local correlated dipoles [15–17]. Structural heterogeneity, caused by chemical substitutions, can introduce local strain gradient ∇S . The local ∇S at the nanoscale deeply impacts the spatial and temperature-dependent evolution of local dipolar moments via flexoelectric effects, and does improve the behaviors of perovskite films and ceramics [18–23]. However, as the contributions of disordered states can barely be distinguished, the exact mechanism by which ∇S contributes

to the behaviors of local correlated dipoles and influences the EO and piezoelectric effects in bulk solid-solution perovskite materials is still unclear.

$\text{KTa}_{1-X}\text{Nb}_X\text{O}_3$ (KTN) is a canonical perovskite solid solution with different B site ions (Ta^{5+} or Nb^{5+}) in ABO_3 lattices. PNRs in KTN yield large quadratic EO effects (approximately 10^{-14} m² V⁻² in magnitude) and excellent nonlinear optical effects (e.g., scale-free optics and reprogrammable soliton nonlinearity) [12,24–27]. In this work, taking KTN as a model system, we investigate the role of ∇S in disorder dynamics and local structure in chemically substituted ferroelectrics. A macroscopic ∇S in the KTN single crystal is designed and achieved by the coupling effect of the Nb-composition gradient ∇X and 180° domains. The manner in which ∇S drives local correlated dipoles is investigated by using the dynamic quadratic EO characteristics. The electric-field-dependent EO results demonstrate the achievement of ∇S and reveal that the ∇S -induced flexoelectric field E_{flexo} is strong enough to control the local dipole moments. Moreover, the crucial degree of ∇S for controlling the disorder dynamics is revealed by dielectric, Raman, and absorption spectroscopies. The local ∇S , caused by random substitutions of B cations, are studied by strain-field analysis at the nanoscale. Based on the pseudo-Jahn-Teller-effect (PJTE) and percolation

*tianhao@hit.edu.cn

theory [17,28], the large local ∇S with a magnitude of approximately 10^{-3} – 10^{-2} nm $^{-1}$ can control local dipole dynamics, deeply contributing to the properties of materials. This work reveals the ∇S -controlled disorder dynamics in chemically substituted ferroelectrics, which provides a basis for the exploration of the origin of the large EO and piezoelectric effects in disordered ferroelectrics.

II. EXPERIMENTAL SECTION

A. Sample preparation and structural characterizations

The KTN single crystal is grown via the top-seeded solution-growth method (please refer to Supplemental Material for the details of the specific process) [29–32]. By controlling the suitable growth conditions, ∇X is achieved along the pulling direction (z direction), and thermal stress is introduced to induce the preferential orientation of polar domains. We extract a $2.30^{(x)} \times 0.90^{(y)} \times 1.00^{(z)}$ mm 3 sample from the as-grown crystal. The x , y , and z directions correspond to the [100], [010], and [001] crystallographic directions, respectively. The central location of the sample along the z direction is defined as $z=0$. All facets of the KTN sample are polished. To inspect microdomain structures, vertical piezoresponse force microscopy (PFM) images are obtained by using a commercial microscope (Cypher ES, Asylum Research) with conductive Pt/Ir-coating probes (EFM, Nanoworld). X-ray diffraction (XRD) with CuK α radiation (X'Pert PRO MPD, PANalytical) is used to detect the phase structure of the single crystal. High-resolution transmission electron microscopy (HRTEM) images are collected by the FEI Talos F200X electron microscope with an accelerating voltage of 200 kV.

B. Strain-gradient-induced features

Silver electrodes are painted onto both xy facets. The temperature dependence of the relative dielectric permittivity (ϵ_r) is measured at 1 kHz with an *LCR* meter (E4980A, Agilent Technologies). T_C values at different locations along the pulling direction are obtained from the graph of ϵ_r vs temperature. The Fröhlich entropy s is calculated from the equation $s = (\epsilon_0 \partial \epsilon_r) / (2\partial T_K)$, where ϵ_0 is the vacuum permittivity and T_K is the absolute temperature, to indicate the ∇S -controlled order-disorder states [15,33]. The dynamic quadratic EO coefficients s_{11} – s_{12} under different ac and (ac + dc) electric fields for a wavelength of 632.8 nm are measured with the Senarmont compensator method in the temperature range of $(T_C - 2^\circ\text{C})$ – $(T_C + 6^\circ\text{C})$ (please refer to Supplemental Material for the EO experimental details and setup) [29,34]. Polarization–electric-field (P – E) hysteresis loops are also measured at 100 Hz and at room temperature T_{room} to reveal the structural features by using a ferroelectric

test system (Precision Premier II, Radiant Technologies Inc.). To further confirm the impact of ∇S on the disorder dynamics, Raman spectra of samples with different compositions are collected on a Renishaw inVia confocal Raman system using a 532-nm laser. Moreover, absorption spectra are recorded with a scientific grade spectrometer (QE65000, Ocean Optics Inc.) and are corrected for reflection losses.

III. RESULTS AND DISCUSSION

A. Design of the strain gradient in the KTN crystal

In the KTN crystal, in addition to the inherent differences in the B site ionic radii, the off-center instability of Nb $^{5+}$ ions can produce local polarization because of the PJTE, while the Ta $^{5+}$ ions remain at the centers of the unit cells, further enlarging the structural heterogeneity near T_C [35–37]. However, macroscopic isotropy in homogeneous samples limits the embodiment of local ∇S -induced inversion symmetry breaking. Here, we create a macroscopic ∇S by the coupling effect of ∇X and 180°-type domains [38]. The as-designed sample has the domain structure and ∇X along the polar axis, as shown in Figs. 1(a) and 1(b), respectively. The 180°-type domains in the tetragonal phase provide a certain polar axis along the z axis. When the temperature is close to the average T_C of the sample, because of the relation between T_C and the Nb-composition fraction X [$T_C = (676X + 32)$ K] [39], the X rich region is in the ferroelectric phase, while the region with poor X is in the paraelectric phase. Therefore, ∇X

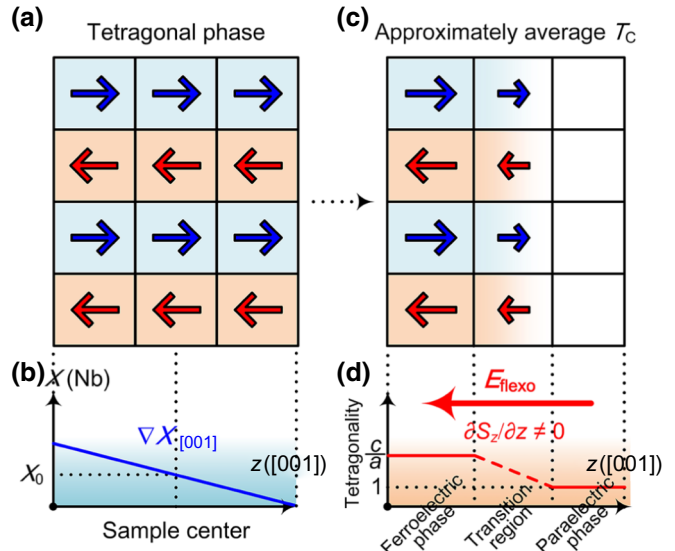


FIG. 1. Design of the strain gradient of $\text{KTa}_{1-X}\text{Nb}_X\text{O}_3$ crystal. (a) 180° domains with average polarization $\langle P \rangle = 0$ at room temperature. (b) Nb-composition gradient ∇X along the $z([001])$ direction. (c) Spatial phase distribution near T_C . (d) Schematic of strain gradient ∇S_z .

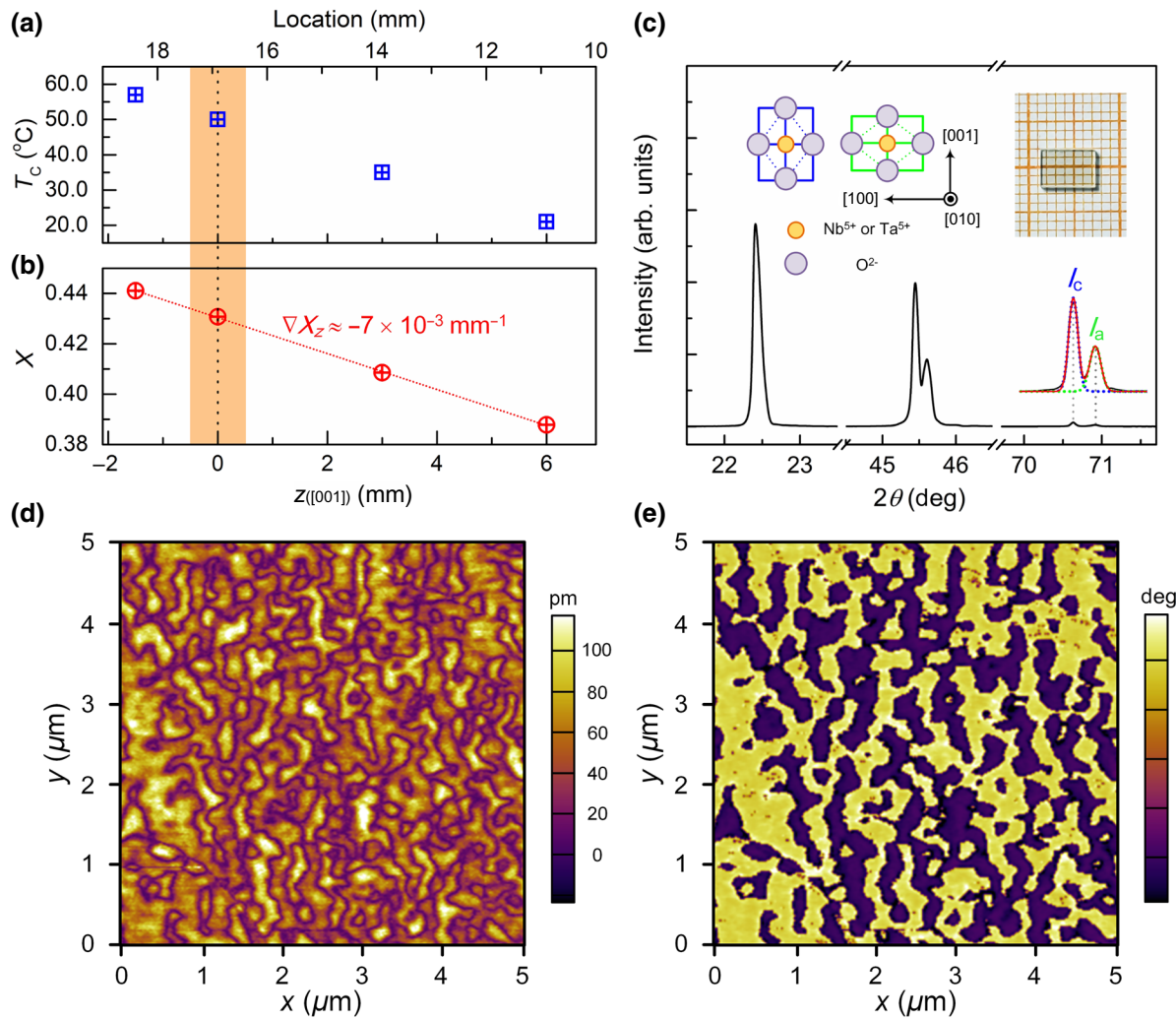


FIG. 2. Nb-composition gradient ∇X_z and tensile-stress-induced domain structures. (a, b) Distributions of T_C and X along the z axis, respectively. The location represents the distance from the growth starting point along the pulling direction. The sample at $z = 0$ with a thickness of 1 mm is used in this work. (c) X-ray ($\lambda = 1.5406 \text{ \AA}$) diffraction pattern collected at the xy facet at T_{room} . The top left blue and green unit structures show the c (polar axis) and a axes of the tetragonal phase perovskite lattices along the [001] crystallographic direction, respectively. For simplicity, only the (010) plane is shown, and apical K cations are omitted. A photograph of the sample at $z = 0$ is shown in the top right. (d, e) Amplitude and phase of PFM images on the xy facet ([001] facet) at T_{room} , respectively.

induces a polarization gradient along the initial polar axis in the transition region, as shown in Figs. 1(c) and 1(d). This gives rise to $\partial S_z / \partial z \neq 0$ in the transition region. The ∇S_z ($\nabla S_z = \partial S_z / \partial z$) provides an internal electric field E_{flexo} ($E_{\text{flexo}} = \mu \nabla S_z / \epsilon$, where μ is the flexoelectric coefficient and ϵ is the dielectric constant) via the flexoelectric effect to drive local dipoles [40,41]. The achieved macroscopic ∇S_z in the transition region can be used for investigating the role of ∇S in chemically substituted ferroelectrics.

The ∇X and 180° -type domains in the KTN sample are the keys to achieving ∇S . Composition gradient engineering, proposed by Tian *et al.*, provides an effective approach to achieve ∇X [30]. Under suitable growth conditions, the controllable segregation effect of Nb^{5+} and Ta^{5+} can yield ∇X along the pulling direction (z direction). Meanwhile,

180° -type domains can also be obtained. In the growth process, the temperature change along the z direction introduces the z direction thermal stress

$$\sigma_z \approx \alpha E W^2 d^2 T / dz^2, \quad (1)$$

where α is the thermal expansion coefficient, E is the elastic modulus, and W is the dimension parameter [42]. In the presence of only σ_z , the elastic Gibbs-free-energy function can be expressed as follows:

$$G = G_0 - h_{11} \sigma_z^2 / 2 - Q_{11} \sigma_z P_z^2 - Q_{12} \sigma_z (P_x^2 + P_y^2), \quad (2)$$

where P_i ($i = x, y, z$) is the polarization along the x , y , and z directions, respectively, G_0 is the only polarization-related

term, h_{11} is the elastic compliance, and Q_{11} and Q_{12} are the electrostrictive constants [43]. σ_z deepens the potential well in the $\pm z$ directions, and induces the preferential orientation of polar domains along the z axis when the sample is in the tetragonal phase. Further, for screening depolarization effects, stable 180° -type domains are formed along the z axis [20].

To achieve the coexistence of ∇X and 180° -type domains, the KTN crystal is designed and grown by controlling suitable growth conditions, especially the growth temperature (see Fig. S1 within the Supplemental Material) [29]. Figure 2(a) shows the T_C at different locations along the z direction measured from the plot of ϵ_r vs temperature. For KTN, T_C has a linear relationship with X . That is, $T_C = (676X + 32)$ K [39]. By using the relation between T_C and X , the X distribution along the z axis is obtained, as shown in Fig. 2(b). The as-grown sample, of which the central position is at $z = 0$, is used in this work. The sample has an average T_C of 50°C ($X = 0.43$) and a ∇X_z ($\nabla X_z = \partial X / \partial z$) of $-7 \times 10^{-3} \text{ mm}^{-1}$. The as-grown sample is in the tetragonal phase at T_{room} (see Fig. S3 within the Supplemental Material) [29]. The amplitude and phase of the PFM images are observed on the xy facet [(001) facet] at T_{room} , as shown in Figs. 2(d) and 2(e), respectively, revealing the 180° -type domains along the z axis. In addition, Figure 2(c) depicts the single-crystal XRD patterns collected at the xy facet at T_{room} . Different lengths of the c and a axes, as shown in the inset of Fig. 2(c), usually yield splitting peaks, where the c axes contribute to the smaller 2θ [44]. Generally, the c axis-induced intensity I_c should be half of the a axis-induced intensity I_a because of the macroscopic inversion symmetry. However, the XRD results reveal that I_c is more than twice I_a , statistically indicating the preferential orientation of dipoles along the z axis.

The above results reveal that large ∇X_z and 180° -type domains along the z axis are both achieved in the as-grown KTN sample. Hence, as shown in the schematic in Fig. 1, the coupling effect of these two factors induces the ∇S_z and E_{flexo} near T_C . The impacts of ∇S_z on the dynamics of local dipoles are investigated in the next section. In addition, the photograph [inset of Fig. 2(c)] shows the high quality and good crystallinity of the as-grown sample.

B. Strain-gradient-induced disorder dynamics

The high sensitivity and accuracy of the EO effect in predicting the dipolar cluster response make it suitable for characterizing polar microregions and investigating correlated disorder systems [45–47]. Here, we demonstrate the achievement of ∇S_z and investigate ∇S_z -triggered disorder dynamics via the electric-field-dependent EO characteristics. Figure 3(a) shows the quadratic EO coefficients $s_{11}-s_{12}$ near T_C (50°C) under different ac electric fields E_{ac} . E_0 is the peak value of E_{ac} and the frequency of E_{ac} is

16 Hz throughout this work. An increasing E_{ac} enhances $s_{11}-s_{12}$. Especially at T_C , $s_{11}-s_{12}$ is enhanced from 1.99×10^{-15} to $3.63 \times 10^{-15} \text{ m}^2 \text{ V}^{-2}$ when E_0 increases from 10 to 40 V mm^{-1} . The quadratic EO effect under (ac + dc) electric fields, as shown in Fig. 3(b), is also investigated by holding E_{ac} constant ($E_0 = 15 \text{ V mm}^{-1}$). The positive E_{dc} is parallel to E_{flexo} . $s_{11}-s_{12}$ manifests asymmetric features when changing the E_{dc} direction near T_C . At T_C , the $+25\text{-V mm}^{-1}$ E_{dc} improves the zero- E_{dc} $s_{11}-s_{12}$ ($2.57 \times 10^{-15} \text{ m}^2 \text{ V}^{-2}$) to $2.73 \times 10^{-15} \text{ m}^2 \text{ V}^{-2}$, while $s_{11}-s_{12}$ is reduced to $2.18 \times 10^{-15} \text{ m}^2 \text{ V}^{-2}$ under a -25-V mm^{-1} E_{dc} . However, after annealing the sample at 450°C slightly above the para-ferroelectric phase-transition temperature of KNbO₃ crystals (435°C) for 10 h and then cooling it to T_{room} at a rate of $0.5^\circ\text{C min}^{-1}$, the strong electric field dependences of the quadratic EO effects disappear in the annealed sample, and a much larger $s_{11}-s_{12}$ ($4.85 \times 10^{-15} \text{ m}^2 \text{ V}^{-2}$ at T_C) is achieved, as shown in Figs. 3(c) and 3(d).

The evolution of quadratic EO characteristics indicate the implementation of ∇S_z and reveal the role of ∇S_z in disorder dynamics. The ∇S_z -induced E_{flexo} yields the strong electric-field-dependent $s_{11}-s_{12}$ in the as-grown sample. The vibration and reorientation of local dipoles both influence the EO properties through the electric susceptibility χ [25,46]. The classical Debye equation for χ of polar units takes into account both contributions,

$$\chi = \chi_d/[1 + (\omega_p \tau_d)^2] + \chi_o/[1 + (\omega_p \tau_o)^2], \quad (3)$$

where χ_d and χ_o are the displacive and orientational electric susceptibilities, respectively, τ_d and τ_o are the corresponding relaxation times, and ω_p is the electric-field frequency [37]. The term χ_o , stemming from the reorientational dynamics of dipolar moments, contributes more to the polarization under low-frequency fields than χ_d . As shown in Fig. 4(a), near the average T_C , E_{flexo} provides an oriented force, which strengthens the correlation of nanosized reconfigurable polar regions (the so-called PNRs) and suppresses the reorientation of the local correlated dipoles. Hence, the formed large-sized dipolar clusters controlled by E_{flexo} reduce the EO effect. The increased E_{ac} activates the confined dipoles and recovers their reorientation modes, which enhances χ_o and $s_{11}-s_{12}$. In addition, the light scattering caused by the large-sized dipolar clusters can limit the modulation of light polarization, inhibiting the EO properties [12]. As shown in Fig. 4(b), under the (ac + dc) electric field, the positive E_{dc} parallel to E_{flexo} further improves the dipolar-cluster-arranging regularity driven by E_{flexo} , diminishing the light scattering and enhancing $s_{11}-s_{12}$. However, E_{dc} (antiparallel to E_{flexo}) breaks the ordered orientations of these dipolar clusters, and the reconstituted balance state yields stronger light scattering and reduces $s_{11}-s_{12}$.

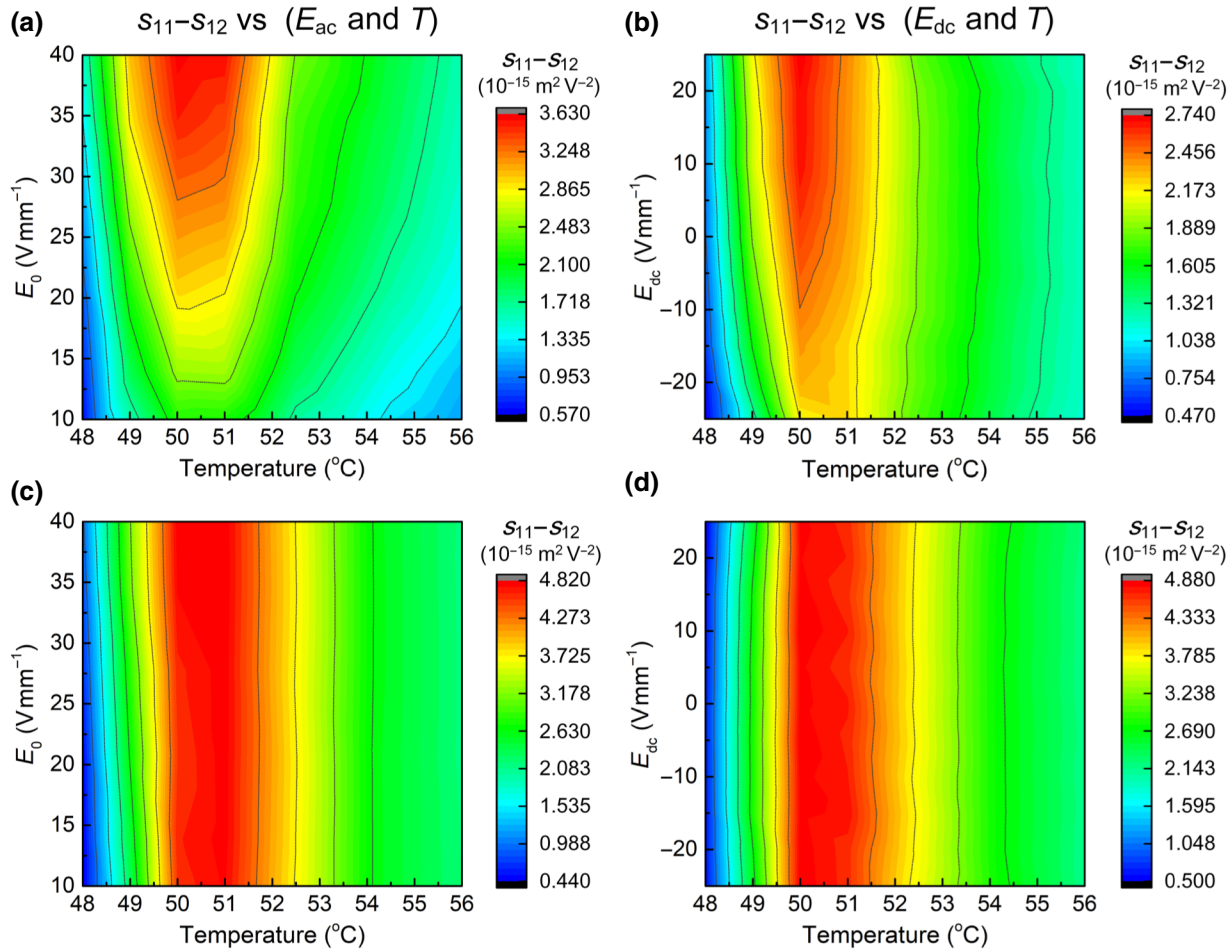


FIG. 3. Electric field and temperature dependences of the quadratic EO coefficient $s_{11}-s_{12}$. $s_{11}-s_{12}$ of the (a, b) as-grown sample and (c, d) annealed sample under ac and (ac + dc) electric fields, respectively. Under the (ac + dc) electric-field conditions, the E_0 of the E_{ac} component is 15 V mm^{-1} . In (b), the positive E_{dc} is parallel to ∇S_z -induced E_{flexo} .

The heat treatment releases the growth-induced thermal stress, effacing the preferential orientation of domains along the z axis. Figure 4(d) shows the partial XRD pattern of the annealed sample collected at the xy facet. The recovered macroscopic inversion symmetry at T_{room} induces an increase in I_a and a decrease in I_c . The variation of I_c/I_a indicates the decrease in the number of 180° -type domains along the z axis. To reduce the stain energy, as shown in Fig. 4(c), more 90° -type domains are formed at T_{room} in the annealed sample [48]. The reconstructed domain structure also greatly weakens the domain clamping effect [49]. Figure 4(e) shows the $P-E$ hysteresis loops at T_{room} before and after the heat treatment, respectively. When a 5 kV cm^{-1} electric field is applied along the z axis, the domain-clamping effect caused by 180° -type domains [Fig. 4(a)] largely limits the polarization (only $4 \mu\text{C cm}^{-2}$) in the as-grown sample, while the annealed KTN has an enhanced polarization of approximately $17 \mu\text{C cm}^{-2}$. The XRD pattern and $P-E$ hysteresis loop of the annealed sample indicate the change in domain structures yielded by

the release of thermal stress. Although ∇X_z still exists, the ∇S_z near T_C vanishes because of the domain structure changes. The absent E_{flexo} weakens the correlation of local dipoles, recovering the nonergodic PNR states near T_C [Fig. 4(c)]. Figure 4(f) shows the temperature dependences of ϵ_r and Fröhlich entropy s . The larger absolute values of s near T_C in the annealed sample indicate that the local correlated dipoles, not confined by ∇S_z -induced E_{flexo} , are easier to drive. The freer state of local dipoles near T_C has a larger χ_o , which induces the enhanced peak ϵ_r of 1.56×10^4 . Hence, the active field-driven reorientations of PNRs enhances χ_o , yielding a much larger $s_{11}-s_{12}$ in the annealed sample. Simultaneously, because of the absence of E_{flexo} , the $s_{11}-s_{12}$ after the heat treatment is independent of the electric field.

The electric-field-dependent EO characteristics in the as-grown sample and their evolutions after the heat treatment clearly indicate that the ∇S_z -induced E_{flexo} is sufficiently strong to control the local dipole moments. ∇S_z provides an oriented force and strengthens the correlation

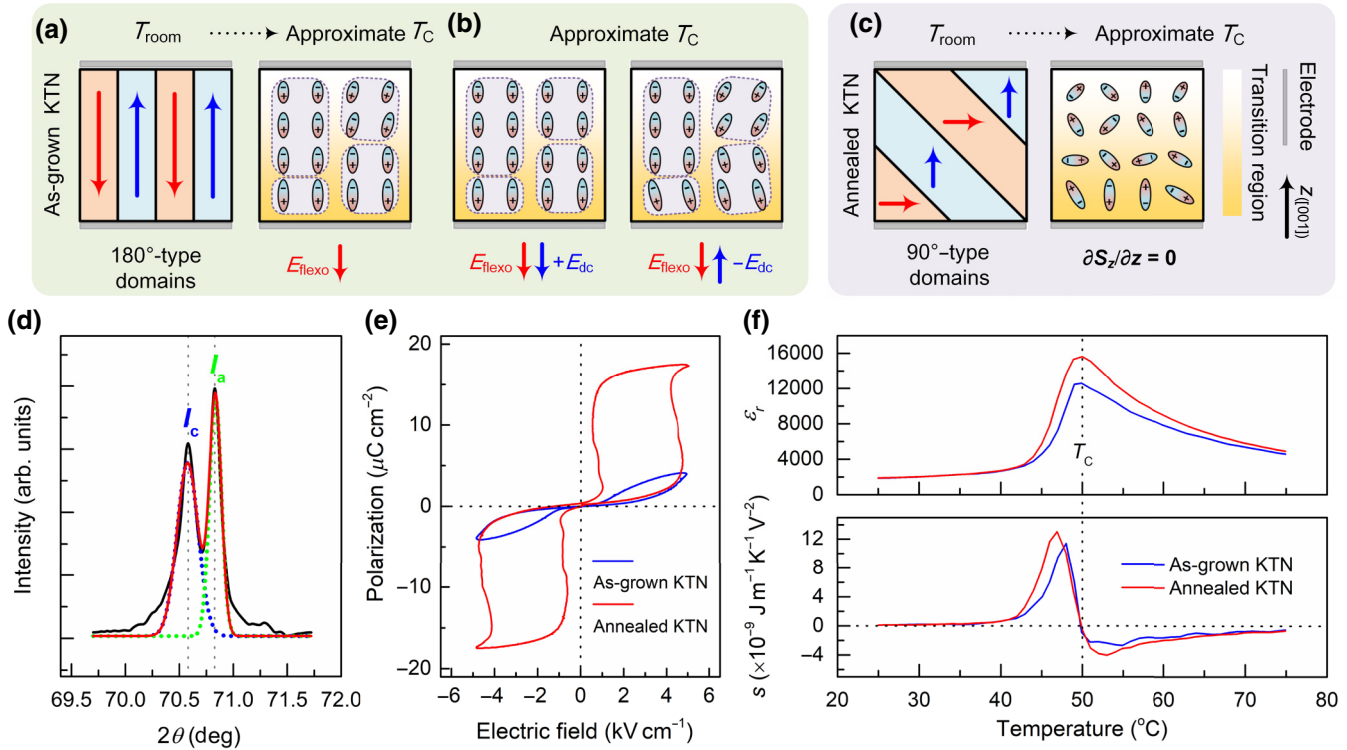


FIG. 4. Heat-treatment-induced changes in structures and properties. (a)–(c) Schematics of microstructures at T_{room} and T_C in the as-grown (green background) and annealed (purple background) KTN, respectively. (d) X-ray ($\lambda = 1.5406 \text{ \AA}$) diffraction pattern collected at the xy facet in the annealed KTN at T_{room} . The black and red lines show the measured and fitted values, respectively. (e) Polarization–electric (P – E) hysteresis loops measured at T_{room} . (f) Temperature dependence of relative dielectric permittivity ϵ_r measured at 1 kHz and Fröhlich entropy s . T_C is 50°C .

of local dipoles. In addition, the differences in s and ϵ_r before and after the heat treatment only occur in the temperature range of $(T_C - 10^{\circ}\text{C})$ – $(T_C + 20^{\circ}\text{C})$, manifesting the effective range of the achieved ∇S_z .

C. The role of the local strain gradient

The local composition and defects can also influence the local dipole dynamics. To reveal their contribution to the dipolar dynamics in the as-grown KTN sample, we conduct the following studies. Raman scattering is beneficial for revealing the lattice dynamics of mixed perovskites. Figure 5(a) shows the Raman spectra of different samples analyzed at T_C . KTN-1 is the sample we use above; KTN-2 ($T_C = 21^{\circ}\text{C}$) is extracted from the same as-grown crystal and has the same ∇X_z as KTN-1. The same ∇S_z in KTN-1 and KTN-2 yields the same PNR-related 196-cm^{-1} Fano resonances and their approximately 555 cm^{-1} TO₄ modes [50–52]. In the annealed KTN-1, the vanished ∇S_z activates PNRs, enhancing the 196- and 555-cm^{-1} mode responses. The result indicates that ∇S has a greater effect on dipole behaviors than the average X value. Oxide ferroelectrics possess a certain density of defects, with the best single crystals possessing defect densities of 10^{17} cm^{-3} [20]. The defects (e.g., oxygen

vacancies) induce intermediate energy levels between the conduction band and valence band, which can be detected through absorption spectra [53,54]. Figure 5(b) shows the absorption spectra measured at $(T_C + 2^{\circ}\text{C})$, where KTN-3 ($T_C = 21^{\circ}\text{C}$) has a relatively uniform composition. All the samples are highly transparent over the spectral ranges (the absorption coefficient $\alpha_0 < 0.15 \text{ cm}^{-1}$). The ultraviolet absorption edges, where α_0 equals 20 cm^{-1} , both lie at $(386 \pm 1) \text{ nm}$ in the same T_C samples. The X difference yields a significant redshift of the band edge, that is, $(392 \pm 1) \text{ nm}$, in the Nb-rich sample. The α_0 results indicate that the large ∇X_z in the as-grown sample induces few extra defect densities [55]. Hence, defect-induced pinning effects for local dipoles are avoided as much as possible. The Raman and absorption spectra reveal that the achieved ∇S , rather than the average X and defects, determines the local dipole dynamics in the as-grown KTN sample.

It is clear that ∇S , caused by the coupling effect of ∇X and 180° -type domains, is sufficiently strong to control the local correlated dipoles. The local ∇S also has prominent roles in the disorder dynamics, because the flexoelectric effect scales inversely with size, and in nanoscale structures, can be engineered to be as large as the piezoelectric effect [19,56]. The structural heterogeneity caused by random substitutions of B cations yields the strong local

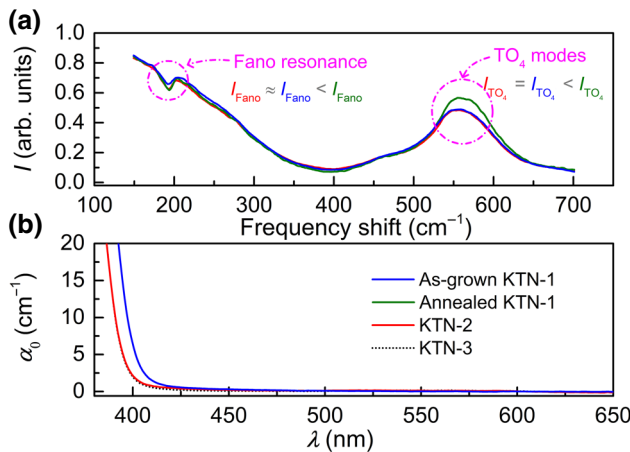


FIG. 5. Raman and absorption spectra. (a) Raman spectra of KTN-1 and KTN-2. The Fano resonance and TO_4 modes are marked. (b) Absorption spectra. KTN-1 is the sample we use above; KTN-2 ($T_C = 21^\circ\text{C}$) is extracted from the same as-grown crystal and has the same ∇X_z as KTN-1; the KTN-3 sample ($T_C = 21^\circ\text{C}$) has a small ∇X_z of $2.63 \times 10^{-3} \text{ mm}^{-1}$.

∇S . Figure 6(a) shows the HRTEM image collected in KTN-1 at T_{room} . To observe the local ∇S , we obtain the detailed distribution of the strain in this imaging region by means of geometric phase analysis (GPA) [57,58]. Following the x axis and y axis in the $[100]$ and $[010]$ orientations, respectively, the strain fields S_{xx} , S_{yy} , shear (S_{xy}), and rotation (Rot) are calculated, as shown in Figs. 6(b)–6(e). Figures 6(f) and 6(g) indicate the S_{xx} and S_{yy} distributions along the black dotted lines in Figs. 6(b) and 6(c), respectively. The local ∇S has a magnitude of approximately 10^{-3} – 10^{-2} nm^{-1} . The inherent differences in the ionic radii and off-center PJTE instability of B site ions

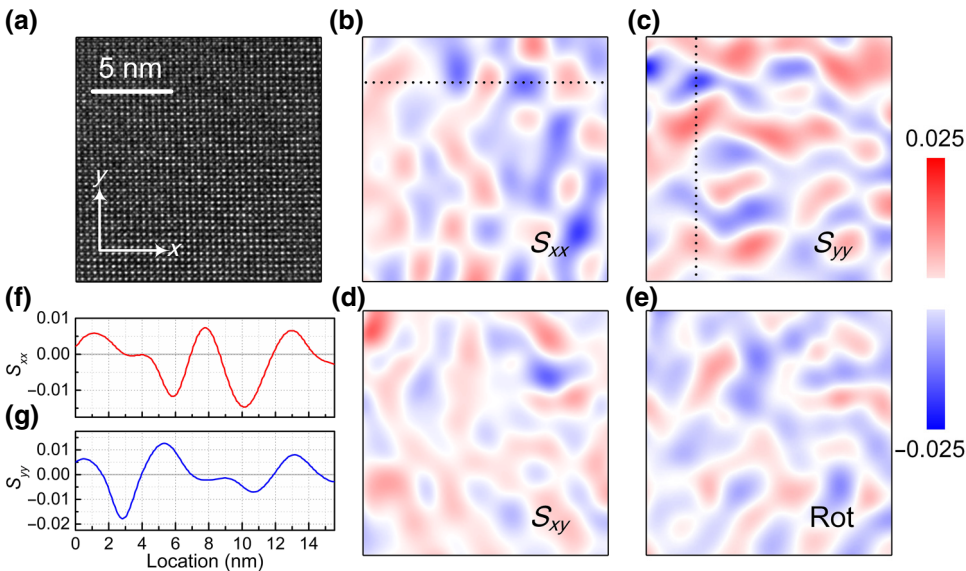


FIG. 6. Local strain gradient ∇S at the nanoscale. (a) HRTEM image of KTN-1 at the scale of 5 nm. (b)–(e) Strain fields along the x axis and y axis (S_{xx} and S_{yy} , respectively), shear (S_{xy}), and rotation (Rot), respectively, obtained by GPA analysis from the HRTEM image shown in (a). (f), (g) S_{xx} and S_{yy} distributions along the black dotted lines in (b) and (c), respectively.

(Nb^{5+} and Ta^{5+}) yield the structural heterogeneity, inducing the local ∇S at the nanoscale. In the vicinity of T_C , local Nb^{5+} -rich regions tend to exhibit tetragonal symmetry, and the calculated c/a ratio is approximately 1.034 [59], while the Ta^{5+} -rich regions exhibit cubic symmetry. The structural symmetry difference can further enlarge the local ∇S near T_C .

Such a large ∇S strongly influences the local dipole dynamics [60]. On the one hand, ∇S eases the condition of the PJTE polar instability and enhances the dynamic Nb-ion (even Ta-ion) distortion. Similar to SrTiO_3 , the virtual ferroelectric KTaO_3 units disobey the condition of dipolar instability, but ∇S can induce their PJTE instability [61]. On the other hand, the E_{flexo} -induced percolation effect causes the correlation of local dipoles and facilitates the formation of nanoscale PNRs or nanodomains [28]. Overall, the local ∇S enhances the PJTE instability and induces the correlation of local dipoles in KTN, which controls the χ and disorder dynamics. These disorder dynamics are different from those of lead-based materials such as $\text{Pb}(\text{Zr}, \text{Ti})\text{O}_3$. Disordered states in $\text{Pb}(\text{Zr}, \text{Ti})\text{O}_3$ are mainly attributed to the Pb distortions triggered by the B cation environment [62]. However, the K cations are inactive in KTN; thus, the local ∇S in a highly polarizable matrix becomes the significant contributor to the correlated disorder. The local ∇S provides a stronger driving force for local dipoles; thus, the reorientations of local correlated dipoles require lower-frequency and larger-amplitude electric fields to activate, yielding strong frequency dispersions and electric-field dependences of the EO effect [46,63]. The local E_{flexo} controls the domain configurations and provides the restoring force, which induces the P – E double loops, as shown in Fig. 4(e) [56,64]. In addition, the characteristics of the sharp-transition relaxor (or incipient relaxor) in KTN (e.g., the weak-frequency-dependent

dielectric susceptibility) may also stem from the local ∇S caused by the structural heterogeneity [10,15,65,66].

IV. CONCLUSIONS

In this work, we successfully design and realize the macroscopic ∇S_z in a KTN single crystal by the coupling effect of ∇X_z and 180°-type domains in the vicinity of T_C . The contributions of ∇S to the disorder dynamics and material properties in the bulk chemically substituted perovskite crystal are investigated by using the directional ∇S sample. The strong electric-field-dependent quadratic EO features reveal the implementation of ∇S_z and the role of ∇S in disorder dynamics. The electric field E_{flexo} , caused by the flexoelectric effect, exhibits directionality and polarity to strongly drive the local dipoles moments, strengthening the correlation of local dipoles and controlling their orientations. Moreover, dielectric, Raman, and absorption spectroscopies indicate that in this work ∇S plays a decisive role in the local dipole dynamics. Strain-field analysis shows that the structural heterogeneity, caused by random substitutions of B cations, yields the local ∇S having a magnitude of approximately 10^{-3} – 10^{-2} nm $^{-1}$. The large local ∇S can ease the condition of the B cation polar instability caused by the PJTE and induces the nanoscale correlation of local dipoles, controlling χ and disorder dynamics. Hence, ∇S is the key to regulating the material properties, especially in chemically substituted ferroelectrics. The investigation of the ∇S -triggered disorder dynamics provides a basis for exploring the origin of the large EO and piezoelectric effects in disordered bulk ferroelectrics. The design and growth methods of the 180°-type domains and macroscopic ∇S in the transition region are valuable for the development of alternative functional bulk materials and devices.

ACKNOWLEDGMENTS

This work was supported by the National Natural Science Foundation of China (Grants No. 11674079 and No. 50902034). The authors wish to thank the Laboratory of Micro-Optics and Photonic Technology of Heilongjiang Province for help with the experiments.

- [1] D. A. Keen and A. L. Goodwin, The crystallography of correlated disorder, *Nature* **521**, 303 (2015).
- [2] P. F. Damasceno, M. Engel, and S. C. Glotzer, Predictive self-assembly of polyhedra into complex structures, *Science* **337**, 453 (2012).
- [3] G. Xu, J. Wen, C. Stock, and P. M. Gehring, Phase instability induced by polar nanoregions in a relaxor ferroelectric system, *Nat. Mater.* **7**, 562 (2008).
- [4] E. Dagotto, Complexity in strongly correlated electronic systems, *Science* **309**, 257 (2005).

- [5] S. J. L. Billinge, T. Proffen, V. Petkov, J. L. Sarro, and S. Kycia, Evidence for charge localization in the ferromagnetic phase of $\text{La}_{1-x}\text{Ca}_x\text{MnO}_3$ from high real-space-resolution x-ray diffraction, *Phys. Rev. B* **62**, 1203 (2000).
- [6] T. Siegrist, P. Jost, H. Volker, M. Woda, P. Merkelbach, C. Schloemann, and M. Wutting, Disorder-induced localization in crystalline phase-change materials, *Nat. Mater.* **10**, 202 (2011).
- [7] F. Yao, K. Wang, W. Jo, K. G. Webber, T. P. Comyn, J. Ding, B. Xu, L. Cheng, M. Zheng, Y. Hou, and J. Li, Diffused phase transition boosts thermal stability of high-performance lead-free piezoelectrics, *Adv. Funct. Mater.* **26**, 1217 (2016).
- [8] E. DelRe, E. Spinozzi, A. J. Agranat, and C. Conti, Scale-free optics and diffractionless waves in nanodisordered ferroelectrics, *Nat. Photonics* **5**, 39 (2011).
- [9] A. V. Ievlev, S. Jesse, A. N. Morozovska, E. Strelcov, E. A. Eliseev, Y. V. Pershin, A. Kumar, V. Ya. Shur, and S. V. Kalinin, Intermittency, quasiperiodicity and chaos in probe-induced ferroelectric domain switching, *Nat. Phys.* **10**, 59 (2013).
- [10] A. A. Bokov and Z.-G. Ye, Recent progress in relaxor ferroelectrics with perovskite structure, *J. Mater. Sci.* **41**, 31 (2006).
- [11] G. Burns and F. H. Dacol, Crystalline ferroelectrics with glassy polarization behavior, *Phys. Rev. B* **28**, 2527 (1983).
- [12] Y.-C. Chang, C. Wang, S. Yin, R. C. Hoffman, and A. G. Mott, Giant electro-optic effect in nanodisordered KTN crystals, *Opt. Lett.* **38**, 4574 (2013).
- [13] T. Zheng, H. Wu, Y. Yuan, X. Lv, Q. Li, T. Men, C. Zhao, D. Xiao, J. Wu, K. Wang, J.-F. Li, Y. Gu, J. Zhu, and S. J. Pennycook, The structural origin of enhanced piezoelectric performance and stability in lead free ceramics, *Energy Environ. Sci.* **10**, 528 (2017).
- [14] M. Zhang, K. Wang, Y. Du, G. Dai, W. Sun, G. Li, D. Hu, H. C. Thong, C. Zhao, X. Xi, Z. Yue, and J. Li, High and temperature-insensitive piezoelectric strain in alkali niobate lead-free perovskite, *J. Am. Chem. Soc.* **139**, 3889 (2017).
- [15] J. Parravicini, E. DelRe, A. J. Agranat, and G. Parravicini, Macroscopic response and directional disorder dynamics in chemically substituted ferroelectrics, *Phys. Rev. B* **93**, 094203 (2016).
- [16] G. A. Samara, The relaxational properties of compositionally disordered ABO_3 perovskites, *J. Phys.: Condens. Mater.* **15**, R367 (2003).
- [17] I. B. Bersuker, Pseudo-Jahn-Teller effect: A two-state paradigm in formation, deformation, and transformation of molecular systems and solids, *Chem. Rev.* **113**, 1351 (2013).
- [18] H. Lu, C.-W. Bark, D. Esque de los Ojos, J. Alcala, C. B. Eom, G. Catalan, and A. Gruverman, Mechanical writing of ferroelectric polarization, *Science* **336**, 59 (2012).
- [19] A. Biancoli, C. M. Fancher, J. L. Jones, and D. Damjanovic, Breaking of macroscopic centric symmetry in paraelectric phases of ferroelectric materials and implications for flexoelectricity, *Nat. Mater.* **14**, 224 (2015).
- [20] A. R. Damodaran, S. Pandya, Y. Qi, S.-L. Hsu, S. Lu, C. Nelson, A. Dasgupta, P. Ercius, C. Ophus, L. R. Dedon, J.

- C. Agar, H. Lu, J. Zhang, A. M. Minor, A. M. Rappe, and L. W. Martin, Large polarization gradients and temperature-stable responses in compositionally-graded ferroelectrics, *Nat. Commun.* **8**, 14961 (2017).
- [21] C. Becher, L. Maurel, U. Aschauer, M. Lilienblum, C. Magén, D. Meier, E. Langenberg, M. Trasslin, J. Blasco, I. P. Krug, P. A. Algarabel, N. A. Spaldin, J. A. Pardo, and M. Fiebig, Strain-induced coupling of electrical polarization and structural defects in SrMnO_3 films, *Nat. Nano* **10**, 661 (2015).
- [22] K. Xu, J. Li, X. Lv, J. Wu, X. Zhang, D. Xiao, and J. Zhu, Superior piezoelectric properties in potassium-sodium niobate lead-free ceramics, *Adv. Mater.* **28**, 8519 (2016).
- [23] G. Catalan, A. Lubk, A. H. G. Vlooswijk, E. Snoeck, C. Magen, A. Janssens, G. Rispens, G. Rijnders, D. H. A. Blank, and B. Noheda, Flexoelectric rotation of polarization in ferroelectric thin films, *Nat. Mater.* **10**, 963 (2011).
- [24] K. Nakamura, J. Miyazu, M. Sasaura, and K. Fujiura, Wide-angle, low-voltage electro-optic beam deflection based on space-charge-controlled mode of electrical conduction in $\text{KTa}_{1-x}\text{Nb}_x\text{O}_3$, *Appl. Phys. Lett.* **89**, 131115 (2006).
- [25] E. DelRe, F. D. Mei, J. Parravicini, G. Parravicini, A. J. Agranat, and C. Conti, Subwavelength anti-diffracting beams propagating over more than 1,000 Rayleigh lengths, *Nat. Photonics* **9**, 228 (2015).
- [26] J. Parravicini, C. Conti, A. J. Agranat, and E. DelRe, Programming scale-free optics in disordered ferroelectrics, *Opt. Lett.* **37**, 2355 (2012).
- [27] D. Pierangeli, A. Tavani, F. D. Mei, A. J. Agranat, C. Conti, and E. DelRe, Observation of replica symmetry breaking in disordered nonlinear wave propagation, *Nat. Commun.* **8**, 1501 (2017).
- [28] S. Prosandeev, D. Wang, A. R. Akbarzadeh, B. Dkhil, and L. Bellaiche, Field-Induced Percolation of Polar Nanoregions in Relaxor Ferroelectrics, *Phys. Rev. Lett.* **110**, 207601 (2013).
- [29] See Supplemental Material at <http://link.aps.org/supplemental/10.1103/PhysRevApplied.11.024037> for details on growth of $\text{KTa}_{1-x}\text{Nb}_x\text{O}_3$ single crystal, characterization of quadratic electro-optic effect, and temperature dependence of relative dielectric permittivity in the range of -150 – 150°C .
- [30] H. Tian, P. Tan, X. Meng, C. Hu, B. Yao, G. Shi, and Z. Zhou, Variable gradient refractive index engineering: design, growth and electro-deflective application of $\text{KTa}_{1-x}\text{Nb}_x\text{O}_3$, *J. Mater. Chem. C* **3**, 10968 (2015).
- [31] H. Tian, P. Tan, X. Meng, C. Hu, G. Shi, Z. Zhou, and X. Wang, Effects of growth temperature on crystal morphology and size uniformity in $\text{KTa}_{1-x}\text{Nb}_x\text{O}_3$ and $\text{K}_{1-y}\text{Na}_y\text{NbO}_3$ single crystals, *Cryst. Growth Des.* **16**, 325 (2016).
- [32] A. Reisman, S. Triebwasser, and F. Holtzberg, Phase diagram of the system KNbO_3 – KTaO_3 by the methods of differential thermal and resistance analysis, *J. Am. Chem. Soc.* **77**, 4228 (1955).
- [33] G. B. Parravicini, M. Campione, F. Marabelli, M. Moret, and A. Sassella, Experimental assessment of nonergodicity in tetracene single crystals, *Phys. Rev. B* **86**, 024107 (2012).
- [34] M. Aillerie, N. Théofanous, and M. D. Fontana, Measurement of the electro-optic coefficients: description and comparison of the experimental techniques, *Appl. Phys. B* **70**, 317 (2000).
- [35] X. Wang, J. Wang, Y. Yu, H. Zhang, and R. I. Boughton, Growth of cubic $\text{KTa}_{1-x}\text{Nb}_x\text{O}_3$ crystal by Czochralski method, *J. Cryst. Growth* **293**, 398 (2006).
- [36] J. Toulouse, F. Jiang, O. Svitelskiy, W. Chen, and Z.-G. Ye, Temperature evolution of the relaxor dynamics in $\text{Pb}(\text{Zn}_{1/3}\text{Nb}_{2/3})\text{O}_3$: A critical Raman analysis, *Phys. Rev. B* **72**, 184106 (2005).
- [37] I. B. Bersuker, Giant permittivity and electrostriction induced by dynamic Jahn-Teller and pseudo Jahn-Teller effects, *Appl. Phys. Lett.* **107**, 202904 (2015).
- [38] A. M. Bratkovsky and A. P. Levanyuk, Formation and rapid evolution of domain structure at phase transitions in slightly inhomogeneous ferroelectrics and ferroelastics, *Phys. Rev. B* **66**, 184109 (2002).
- [39] T. Sakamoto, K. Nakamura, K. Fujiura, and Y. Cho, Spatial distribution of phase transition temperature of $\text{KTa}_{1-x}\text{Nb}_x\text{O}_3$ measured using scanning nonlinear dielectric microscopy, *Appl. Phys. Lett.* **90**, 222908 (2007).
- [40] D. Lee, B. C. Jeon, A. Yoon, Y. J. Shin, M. H. Lee, T. K. Song, S. D. Bu, M. Kim, J.-S. Chung, J.-G. Yoon, and T. W. Noh, Flexoelectric control of defect formation in ferroelectric epitaxial thin films, *Adv. Mater.* **26**, 5005 (2014).
- [41] J. Zhang, R. Xu, A. R. Damodaran, Z.-H. Chen, and L. W. Martin, Understanding order in compositionally graded ferroelectrics: Flexoelectricity, gradient, and depolarization field effects, *Phys. Rev. B* **89**, 224101 (2014).
- [42] O. A. Louchev, S. Kumaragurubaran, S. Takekawa, and K. Kitamura, Thermal stress inhibition in double crucible Czochralski large diameter crystal growth, *J. Cryst. Growth* **274**, 307 (2005).
- [43] T. Yamamoto and H. Matsuoka, Crystallographic and ferroelectric properties subjected to two-dimensional stress in *c*-axis-oriented PbTiO_3 thin films, *Jpn. J. Appl. Phys.* **33**, 5317 (1994).
- [44] K. Wang and J.-F. Li, Domain engineering of lead-free Li-modified (K, Na) NbO_3 polycrystals with highly enhanced piezoelectricity, *Adv. Funct. Mater.* **20**, 1924 (2010).
- [45] D. Pierangeli, F. D. Mei, J. Parravicini, G. B. Parravicini, A. J. Agranat, C. Conti, and E. DelRe, Observation of an intrinsic nonlinearity in the electro-optic response of freezing relaxors ferroelectrics, *Opt. Mater. Express* **4**, 1487 (2014).
- [46] P. Tan, H. Tian, C. Mao, C. Hu, X. Meng, L. Li, G. Shi, and Z. Zhou, Field-driven electro-optic dynamics of polar nanoregions in nanodisordered $\text{KTa}_{1-x}\text{Nb}_x\text{O}_3$ crystal, *Appl. Phys. Lett.* **111**, 012903 (2017).
- [47] W. Zhu, J. Chao, C. Chen, S. Yin, and R. C. Hoffman, Three order increase in scanning speed of space charge-controlled KTN deflector by eliminating electric field induced phase transition in nanodisordered KTN, *Sci. Rep.* **6**, 33143 (2016).
- [48] R. W. Cahn, Twinned crystals, *Adv. Phys.* **3**, 363 (1954).
- [49] M. E. Drougard and D. R. Young, Domain clamping effect in barium titanate single crystals, *Phys. Rev.* **94**, 1561 (1954).
- [50] M. M. Rahaman, T. Imai, T. Sakamoto, S. Tsukada, and S. Kojima, Fano resonance of Li-doped $\text{KTa}_{1-x}\text{Nb}_x\text{O}_3$ single crystals studied by Raman scattering, *Sci. Rep.* **6**, 23898 (2016).

- [51] S. K. Manlief and H. Y. Fan, Raman Spectrum of $\text{KTa}_{0.64}\text{Nb}_{0.36}\text{O}_3$, *Phys. Rev. B* **5**, 4046 (1972).
- [52] M. M. Rahaman, T. Imai, J. Miyazu, J. Kobayashi, S. Tsukada, M. A. Helal, and S. Kojima, Relaxor-like dynamics of ferroelectric $\text{K}(\text{Ta}_{1-x}\text{Nb}_x)\text{O}_3$ crystals probed by inelastic light scattering, *J. Appl. Phys.* **116**, 074110 (2014).
- [53] F. Lüdtke, N. Waasem, K. Buse, and B. Sturman, Light-induced charge-transport in undoped LiNbO_3 crystals, *Appl. Phys. B* **105**, 35 (2011).
- [54] B. A. Wechsler and M. B. Klein, Thermodynamic point defect model of barium titanate and application to the photorefractive effect, *J. Opt. Soc. Am. B* **5**, 1711 (1988).
- [55] S. Torbrügge, M. Imlau, B. Schoke, C. Merschjann, and O. F. Schirmer, Optically generated small electron and hole polarons in nominally undoped and Fe-doped KNbO_3 investigated by transient absorption spectroscopy, *Phys. Rev. B* **78**, 125112 (2008).
- [56] D. Lee and T. W. Noh, Giant flexoelectric effect through interfacial strain relaxation, *Phil. Trans. R. Soc. A* **370**, 4944 (2012).
- [57] M. J. Höstch, E. Snoeck, and R. Kilaas, Quantitative measurement of displacement and strain fields from HREM micrographs, *Ultramicroscopy* **74**, 131 (1998).
- [58] *GPA Phase plug-in for DigitalMicrograph (Gatan)* (HREM Research Inc.) available at: <http://www.hremresearch.com>.
- [59] L. F. Wan, T. Nishimatsu, and S. P. Beckman, The structural, dielectric, elastic, and piezoelectric properties of KNbO_3 from first-principles methods, *J. Appl. Phys.* **111**, 104107 (2012).
- [60] P. Gao, S. Yang, R. Ishikawa, N. Li, B. Feng, A. Kumamoto, N. Shibata, P. Yu, and Y. Ikuhara, Atomic-Scale Measurement of Flexoelectric Polarization at SrTiO_3 Dislocations, *Phys. Rev. Lett.* **120**, 267601 (2018).
- [61] I. B. Bersuker, Pseudo Jahn-Teller effect in the origin of enhanced flexoelectricity, *Appl. Phys. Lett.* **106**, 022903 (2015).
- [62] I. Grinberg, V. R. Cooper, and A. M. Rappe, Relationship between local structure and phase transitions of a disordered solid solution, *Nature* **419**, 909 (2002).
- [63] H. Tian, B. Yao, L. Wang, P. Tan, X. Meng, G. Shi, and Z. Zhou, Dynamic response of polar nanoregions under an electric field in a paraelectric $\text{KTa}_{0.61}\text{Nb}_{0.39}\text{O}_3$ single crystal near the paraferroelectric phase boundary, *Sci. Rep.* **5**, 13751 (2015).
- [64] D. Lee, A. Yoon, S. Y. Jang, J.-G. Yoon, J.-S. Chung, M. Kim, J. F. Scott, and T. W. Noh, Giant Flexoelectric Effect in Ferroelectric Epitaxial Thin Films, *Phys. Rev. Lett.* **107**, 057602 (2011).
- [65] C. Stock, P. M. Gehring, G. Xu, D. Lamago, D. Reznik, M. Russina, J. Wen, and L. A. Boatner, Fluctuating defects in the incipient relaxor $\text{K}_{1-x}\text{Li}_x\text{TaO}_3$ ($x = 0.02$), *Phys. Rev. B* **90**, 224302 (2014).
- [66] V. V. Shvartsman and D. C. Lupascu, Lead-free relaxor ferroelectrics, *J. Am. Ceram. Soc.* **95**, 1 (2012).